Systematics of 0° neutron production by 800 MeV protons on targets with $27 \leq A \leq 238$*

B. E. Bonner and J. E. Simmons
Los Alamos Scientific Laboratory, University of California, Los Alamos, New Mexico 87545

C. R. Newsom and P. J. Riley
University of Texas, Austin, Texas 78712

G. Glass, J. C. Hiebert, Mahavir Jain,† and L. C. Northcliffe
Texas A&M University, College Station, Texas 77843

(Received 11 January 1978)

The 0° neutron spectra resulting from 800 MeV proton bombardment of targets of Al, Ti, Cu, W, Pb, and U have been measured for neutron momenta above 500 MeV/c. Integrated cross sections for the quasielastic charge exchange peaks and the broad pion associated peaks at lower momenta show a remarkably smooth dependence on atomic mass of the target, varying as $A^{2/3}$ and $A^{1/2}$, respectively.

[NUCLEAR REACTIONS Al, Ti, Cu, W, Pb, U(p,n), E=800 MeV; measured σ (0°; P_n); deduced A dependence of charge exchange and pion associated cross sections.]

I. INTRODUCTION

We report here absolute measurements of the 0° neutron spectra produced by 800 MeV proton collisions with targets of Al, Ti, Cu, W, Pb, and U. The resolution attained in the measurement of the neutron momentum is considerably better than has been possible in previous experiments at medium energy. In previous publications we have reported 0° neutron spectrum measurements from targets of H (Ref. 1), ^{2}H (Ref. 2), ^{6}Li and ^{7}Li (Ref. 3), and Be, C, and Al.[4] The present work extends those measurements to heavier targets, thus allowing a study of the systematics of 0° neutron production at 800 MeV.

Previous experiments covering the mass region here have either been at energies below 150 MeV (Refs. 5 and 6) or at angles far from 0° (Ref. 7) with the exception of a recent 0° measurement[8] on Cu at 724 MeV. This measurement suffered from poor energy resolution and statistical uncertainties which severely limits the value of the data.

In our previous studies[1-4] with low mass targets, we have found that the 0° neutron spectrum from all targets (with the exception of hydrogen) is characterized by a strong narrow peak at an energy very close to that of the incident proton beam. This peak is due to a quasielastic charge exchange (CEX) reaction involving the incident proton and one of the neutrons of the nucleus. On the low side of the peak, particularly for C and Al, a shoulder is observed at a momentum corresponding to excitation in the residual nuclei of about 30 MeV and is attributed to a collective effect—possibly the analog of a giant dipole excitation as has often been reported at lower incident energies. About 100 MeV below the peak, a valley is observed followed by a broad [~300 MeV/c full width at half maximum (FWHM)] intense peak centered around 1060 MeV/c. This peak we attribute to neutrons associated with quasifree pion production via the reactions p"n" $\rightarrow np\pi^0$, p"n" $\rightarrow nn\pi^+$, and p"p" $\rightarrow np\pi^+$, where "n" or "p" indicates a nucleon within the nucleus. The dependence of the integral of the cross section for the CEX and pion regions of the spectra on mass of the target nuclei was found to be erratic and not particularly well defined for the low mass ($A \leq 27$) targets, probably because of the strong influence of the few available final states in these light target reactions.

Considerable effort has been expended on intranuclear cascade calculations for the prediction of reaction products from proton collisions with nuclei.[9,10] Previously, we compared the Al(p,n) spectrum[4] at 647 MeV to the prediction of the Brookhaven intranuclear cascade code ISOBAR. Reasonably good agreement was found near the peak of the pion production region around 900 MeV/c; poor agreement was found both at lower and higher momenta. Further comparisons between experiment and the predictions of the code have not been made, but it does appear desirable to modify the theoretical formulation to allow better overall agreement between theory and experiment.

II. EXPERIMENTAL APPARATUS AND METHODS

The experimental arrangement is the same as that used in our previously reported measurements.[1-4] The solid targets were mounted on a remotely

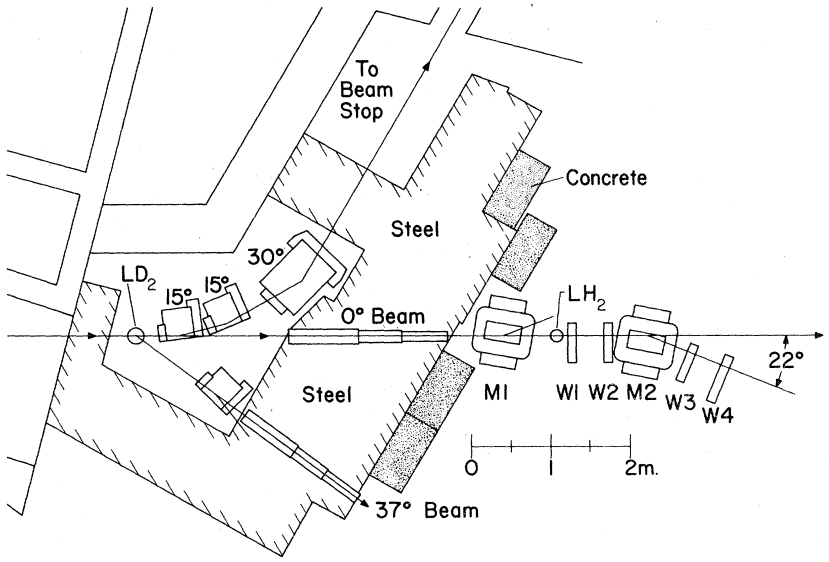

FIG. 1. Plan view of the experimental setup used for the present measurements. The targets were mounted at the location indicated by LD_2 in the figure.

rotatable target wheel which was used to position any one of the targets in the 800-MeV proton beam from the Clinton P. Anderson Meson Physics Facility (LAMPF). A plan view of the experimental setup is shown in Fig. 1. After passing through the target, the proton beam is deflected through 60° and transported to a heavily shielded beam dump several meters away. Neutrons emerging at 0° were collimated to a cone of half angle 0.1° and after passing through the clearing magnet $M1$ encountered a liquid hydrogen radiator of thickness 0.93 g/cm^2 placed upstream of a multiwire proportional chamber (MWPC) spectrometer.

The basic technique used to deduce the momentum spectrum of the neutrons is to measure the spectrum of protons elastically scattered near 0° into the acceptance of the spectrometer, then to take into account the cross section for this process as a function of incident neutron momentum. Corrections and complications which arise in using this technique are as follows: (1) inelastic processes in the radiator leading to a proton in the final state, primarily pion associated protons from the reactions $np \to pn\pi^0$ and $np \to pp\pi^-$; (2) processes leading to other charged particles in the final state, arising from reactions such as $np \to d\pi^0$ and $np \to d\gamma$; (3) events originating in material other than the LH_2 target (i.e., the target flask and vacuum jacket as well as the scintillator $S1$ placed in the neutron beam); (4) knowledge of the np scattering cross section as a function of momentum and angle.

Before discussing the points mentioned above, we first describe the MWPC spectrometer used to measure the proton momentum spectrum. The spectrometer consists of a large dipole magnet ($M2$), four horizontal-vertical (Y-X) pairs of MWPC's ($W1$-$W4$) and two thin scintillators ($S1$, $S2$). The scintillators were positioned just before $W1$ and just after $W4$, respectively. An event is accepted for processing when signals from the two scintillators and at least three out of four of both the X and Y chambers are in coincidence. Data recorded for each event include: (1) the time of flight of the particle over the 4.9-m distance between $S1$ and $S2$, (2) the time of the event with respect to the 5-nsec microstructure of the proton beam, (3) pulse heights in both $S1$ and $S2$, and (4) addresses of active wires in each of the chambers which participated in the event. The wire addresses enable a determination of the charged particle trajectory before and after deflection in the magnet. Since the magnetic field is well known, the path of the particle through the spectrometer can be reconstructed and its momentum deduced, even in the absence of one X and one Y plane. The resolution of the momentum determination is about 1% FWHM.

The geometric acceptance of the spectrometer is limited vertically by the magnet pole pieces and horizontally by the edges of $W3$ and $W4$. For a given magnet current there is a safe region in momentum and in the coordinate space of polar and azimuthal angles θ and φ in which the particle trajectory is certain to intersect the active region of each chamber and in addition to avoid striking the magnet poles. The vertical limits on the acceptance were determined to be $\sin\theta \sin\phi \leq 0.02$. The

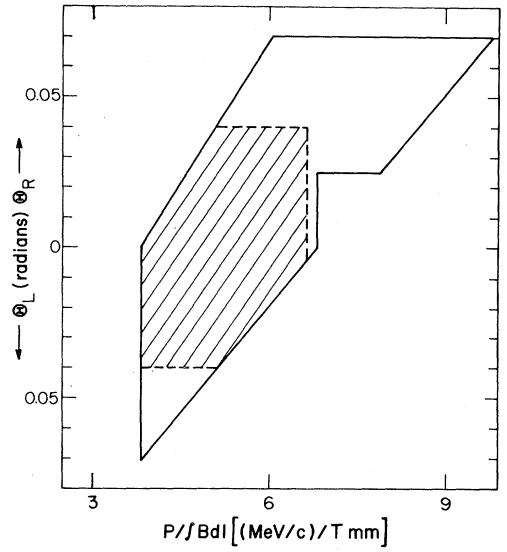

FIG. 2. Acceptance region of the spectrometer. The solid line encloses the region of left (θ_L) and right (θ_R) scattered particles as a function of momentum (normalized to field strength) which are certain to pass through the active volume of the four MWPC's in the spectrometer. The dashed lines show the further restriction imposed on the data reported here to enable direct comparison of overlapping momentum regions taken at different magnet currents.

actual limits on θ for left (θ_L) and right (θ_R) scattered particles are dependent on the momentum of the particle for a given current in the spectrometer magnet. These limits, determined from examination of plots of θ versus momentum for those particles striking the edge wires of $W3$ and $W4$, are indicated by the solid lines in Fig. 2. Particles falling within the enclosed acceptance region and satisfying the vertical limits mentioned above are certain to pass through the safe region of the spectrometer.

The measurement of the complete momentum spectrum from 500 to 1500 MeV/c requires the use of several different magnet currents. In order to be able to check for consistency in the measurement of the spectrum, these currents were chosen to provide some overlap in the momentum ranges covered by the different currents. If the full acceptance of Fig. 2 is utilized, however, a direct comparison cannot be made since at different currents particles of the same momentum are detected over quite different angular ranges. In order to avoid the necessity of knowing in detail the angular distribution of np elastic scattering as a function of momentum before this simple consistency check can be made, a further restriction is applied to the acceptance region in Fig. 2. For a given magnet current only that range of momentum is utilized over which a range of θ from 0 to some value θ_{max} was completely within the acceptance region on either the left or right side of the spectrometer. By choosing θ_{max} to be 0.04 rad we see that the range of $P/\int Bdl$ is 3.91 to 6.65. The actual acceptance region utilized for the measurements reported here is shown by the dashed lines in Fig. 2. For the final spectra at each magnet current setting, the acceptance is effectively "squared up" by applying a weight of 2 to those events at a given point in the acceptance region $(p, \theta_{L(R)})$ if the reflected point $(p, \theta_{R(L)})$ lies outside the acceptance region and a weight of 1 otherwise. This procedure allows direct comparison of the overlapping momentum regions for data taken at different magnet currents as well as simplifying considerably the subsequent correction made necessary by the np cross section variation. The acceptance region spans a wide momentum range ($\Delta P/\overline{P} \simeq 0.52$) for a given current.

The measurement of the time of flight of the particle through the spectrometer in conjunction with momentum allows direct calculation of particle mass by the relation $M = P/\beta\gamma$. A typical mass

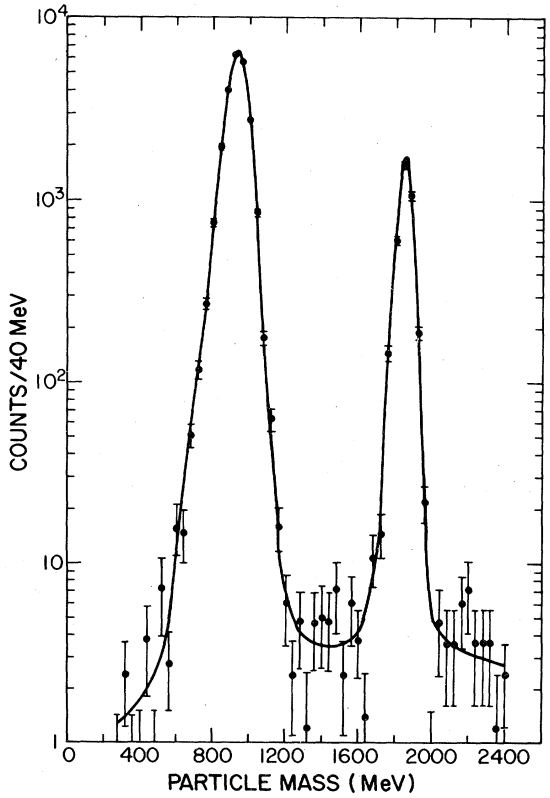

FIG. 3. Mass spectrum of particles detected in the spectrometer for a particular magnet current. The mass associated with each event is calculated from the measured momentum and time of flight through the spectrometer according to the usual relation $M = P/\beta\gamma$.

spectrum is shown in Fig. 3 for a high setting of the magnet current, where the mass resolution is worst. The separation between proton and deuterons is adequate to provide unambiguous identification of particle type. At lower current settings pions and positrons are observed but again are well separated from the protons in the mass spectra.

A fraction of the protons at lower momentum arise from inelastic np interactions in the target volume, predominately the two reactions $np \rightarrow pn\pi^0$ and $np \rightarrow pp\pi^-$. Since only the proton is detected in this experiment, it cannot be determined directly whether the proton is produced from an elastic or inelastic interaction. In order to correct for this inelastic background, a small amount of data was taken using the chopped mode of operation at LAMPF. The microstructure of the LAMPF beam has a 5-nsec period, but this mode suppresses seven out of each eight micropulses and allows a useful measurement of the incident neutron time of flight to be made. By correlating the measured proton momentum with this time of flight, the inelastic events are well separated from the elastic ones of interest. Since chopped beam data were accumulated only with the Al target for a small fraction of the total data, a general prescription was devised to apply a correction factor to the remainder. From the measured time of flight the momentum of the incident neutron was calculated and the chopped data were then sorted into 150-MeV/c-wide bins extending downwards from 1500 to 750 MeV/c (below pion production threshold). The proton momentum spectrum associated with each incident neutron momentum bin was then histogrammed, thus giving the relative inelastic contribution for all proton momenta. These inelastic spectra were then subtracted sequentially, with appropriate normalizations, beginning with the inelastic proton spectrum associated with the highest neutron momentum bin. The correction is dependent both on the spectral shape and momentum and ranges from 0 at the highest momenta to typically 15 to 25% at the lowest proton momenta. The correction for the Al spectrum is shown in Fig. 4. The upper curve shows the final neutron spectrum and the lower curve gives the amount that was subtracted to account for the inelastic reactions in the radiator.

Interactions of the neutron beam in the target flask and vacuum jacket (0.51 mm Mylar) as well as the scintillator $S1$ (1.6 mm) represent sources of background protons in the measured spectra. About 25% of the data for each production target and magnet current were taken with the flask emptied of liquid hydrogen and these data were normalized and subtracted from the corresponding

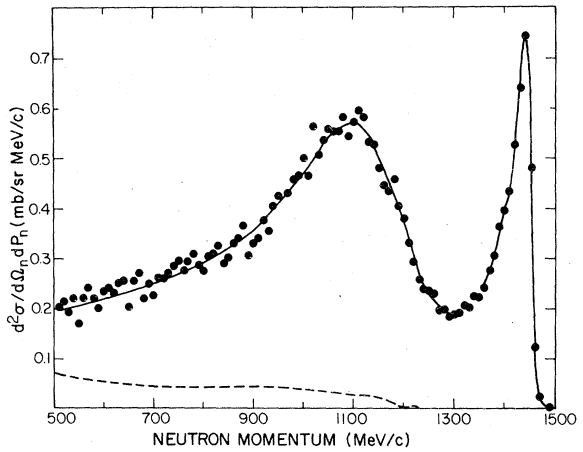

FIG. 4. 0° neutron spectrum arising from 800-MeV proton bombardment of an aluminum target. The dashed curve gives the amount that was subtracted in order to account for inelastic reactions in the liquid hydrogen radiator (see text).

run taken with radiator full. The amount of background subtracted varied with target and momentum but was typically 3–6%.

Conversion of a recoil proton spectrum to a neutron spectrum is accomplished by using the following relationships. The number of protons detected in each momentum bin is given by $Y_p(P_p) = I_n(P_n) n_H \Delta\sigma_{np}(P_n)$, where $I_n(P_n)$ is the number of incident neutrons in the momentum bin centered at P_n giving rise to protons in the bin centered at P_p, n_H is the number of protons/cm^2 in the LH_2 radiator, and $\Delta\sigma_{np}(P_n)$ is the integral over the solid angle subtended by the spectrometer acceptance of the np charge exchange differential cross section at neutron momentum P_n. The quantity $\Delta\sigma_{np}(P_n)$ is defined as follows,

$$\Delta\sigma_{np}(P_n) = \int_0^{0.04} \int \frac{d\sigma^{\mathrm{CEX}}}{d\Omega}(\theta, P_n) \sin\theta \, d\phi \, d\theta,$$

where $(d\sigma^{\mathrm{CEX}}/d\Omega)(\theta, P_n)$ is the np charge exchange differential cross section at proton angle θ and neutron momentum P_n. The integration over ϕ is subject to the constraint that $\sin\theta \sin\phi \leq 0.02$, which leads to the integral

$$\Delta\sigma_{np}(P_n) = 2\pi \int_0^{0.04} \epsilon(\theta) \frac{d\sigma^{\mathrm{CEX}}}{d\Omega}(\theta, P_n) \sin\theta \, d\theta,$$

with

$$\epsilon(\theta) = 1 \text{ for } \theta \leq 0.02$$

and

$$\epsilon(\theta) = \frac{2}{\pi} \sin^{-1}\left(\frac{0.02}{\theta}\right) \text{ for } \theta > 0.02.$$

Thus we require the np differential cross section

TABLE I. Targets and thicknesses used for the present measurements.

Target	Thickness (g/cm^2)
Al	2.74
Ti	2.40
Cu	1.34
W	1.43
Pb	1.84
U	1.78

for $\theta = 0$ to 0.04 and $P_n = 500$ to 1450 MeV/c. In previous publications of this group,[1-4] we have taken the few reported measurements over this range and made a straight line fit to the $\Delta\sigma_{np}(P_n)$ calculated from selected measurements. Recently, however, we reported[11] measurements of the np differential cross section from 800 to 1450 MeV/c in steps of 30 MeV/c. Using the result of those measurements and certain lower energy measurements, we find that the $\Delta\sigma_{np}(P_n)$ used in Refs. 1–4 is in agreement with our more recent results to within 5% and therefore, we use the same prescription for $\Delta\sigma_{np}$ (adjusted for the larger solid angle used in the present measurements),

$$\Delta\sigma_{np}(P_n) = -2.173 \times 10^{-5} P_n + 0.173 \text{ mb}.$$

In order to convert the neutron intensity distribution $I_n(P_n)$ into a cross section $d^2\sigma/d\Omega_n dP_n$ for neutron production, we use the following formula:

$$\frac{d^2\sigma}{d\Omega_n dP_n} = \frac{I_n(P_n)}{I_p n_T \Delta\Omega_n \Delta P_n},$$

where

I_p is the proton current that passed through the production target,
n_T is the number of production target atoms/cm^2 in the beam,
$\Delta\Omega_n$ is the solid angle defined by the neutron collimator, and
ΔP_n is the neutron momentum bin width.

The number of protons passing through the target is determined by integrating the current induced in a toroid[12] through which the proton beam passes just upstream of the production target. Calibration of this device is accomplished electronically and also by comparison with radioactivity induced in an Al foil. The absolute error associated with the calibration is estimated to be ±10%, but for a short time period (~8 h) such as the one when the present data were taken, the relative error associated with the integration system is estimated to be ±4%.

The neutron collimator solid angle is calculated geometrically and corrected for the semitransparency of the edges to neutrons. This correction is calculated to be only 3%.

Both the thickness and density of each target are measured. In each case the measured density agrees with the tabulated density of the elements to within 2%. The thicknesses of the targets used in the present experiment are given in Table I.

The various sources of error and the estimate of each are given in Table II. The two columns refer to absolute normalization error and to the relative error in comparing spectra from two different targets. Adding the individual errors in quadrature, the absolute normalization error is estimated to be ±13% and the relative error between spectra is ±4.5%.

III. RESULTS AND DISCUSSION

The 0° neutron spectra resulting from 800-MeV proton bombardment of the six targets used in the present experiment are shown in Fig. 5. The indicated errors are those due to statistics only. The similarity in shape of these spectra to those reported previously[1-4] is rather striking. All are characterized by a narrow peak at a momentum near that of the proton beam and at lower momenta a broad peak centered around 1080 MeV/c. The upper peak is due to quasielastic charge exchange (CEX) in the nucleus: p"n"$\rightarrow np$. The lower peak is about 300 MeV/c wide and is thought to be due to quasifree pion production: p"n"$\rightarrow nN\pi$. Again, a noticeable shoulder is observed on the low momentum side of the narrow peak in Al as was mentioned in Ref. 4. Additionally, the spectra from

TABLE II. Sources of error and estimates of their magnitude.

Error source	Absolute error (%)	Relative error (%)
Current integration	±10	±4
np cross section	± 8	0
Production target thickness	± 2	±2
Radiator target thickness	± 2	0
Neutron solid angle	± 2	0
Quadrature sum	13.3	4.5

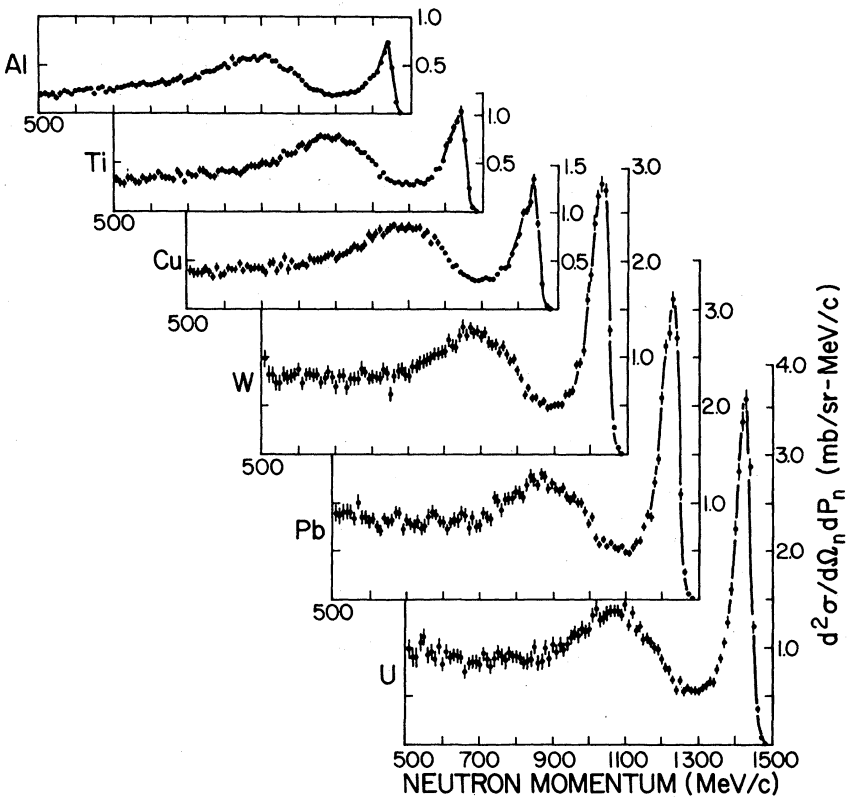

FIG. 5. Neutron spectra observed at 0° from 800-MeV proton interactions with targets of (from the bottom): U, Pb, W, Cu, Ti, and Al. The scales are the same but displaced for both axes.

Ti and Cu manifest a similar shoulder but the structure is not apparent for the higher mass targets.

In order to ascertain any systematic trends as a function of target mass that may be present in the data, the cross section for the CEX and pion regions were integrated over momentum. The momentum value used to divide the two regions was arbitrarily taken to be 1295 MeV/c. The integrals over the two regions for the six targets are given in Table III along with the average values of atomic mass ($\bar{A}$), neutron number ($\bar{N}$), and atomic number (Z). An additional entry is given for the average cross section in the valley (1270–1320 MeV/c) between the two peaks. The results for the CEX and pion region cross sections are plotted versus atomic mass in Fig. 6. Also plotted there are the previous results[1-4] of our group from targets with $A \leq 27$. Although the earlier measurement for Al was made almost two years earlier, the agreement with the present result is well within the systematic errors associated with the two measurements.

The rather smooth dependence on atomic mass

TABLE III. Cross section integrals $[\int (d^2\sigma/d\Omega_n\, dp)\, dP]$ for the charge exchange region ($P_n >$ 1295 MeV/c) and pion associated region ($P_n <$ 1295 MeV/c) in mb/sr. The average cross section in mb/[sr(MeV/c)] observed in the valley between the two peaks is also given. Errors shown are due to counting statistics only.

Target	$\bar{A}$	$\bar{N}$	Z	CEX	Valley	Pion
Al	27.0	14.0	13	58.0 ±0.7	0.19 ±0.01	271.4 ±2.0
Ti	47.9	25.9	22	88.4 ±1.0	0.29 ±0.02	372.1 ±2.7
Cu	63.5	34.5	29	105.4 ±1.2	0.30 ±0.02	425.0 ±3.2
W	183.9	109.9	74	222.0 ±2.3	0.50 ±0.03	695.5 ±5.6
Pb	207.2	125.2	82	225.8 ±2.3	0.50 ±0.03	695.4 ±5.5
U	238.0	146.0	92	252.4 ±2.7	0.55 ±0.04	767.9 ±6.3

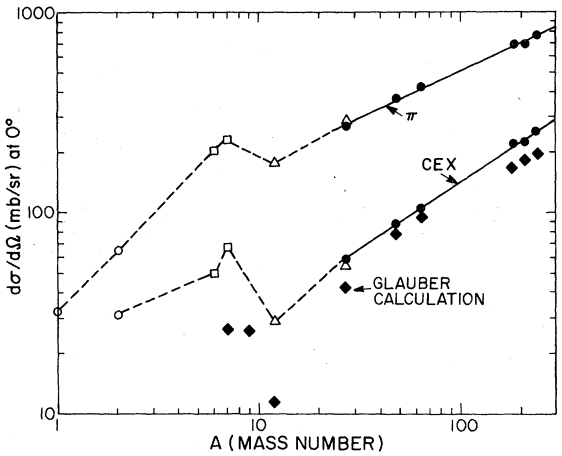

FIG. 6. Plot of the integrals of the charge exchange and pion associated regions of the neutron spectra shown in Fig. 5 versus atomic mass of the production target. The momentum used to divide the two regions was 1295 MeV/c. The solid lines give the results of the power law fits to the present data (solid circles) for the two regions. Also shown are our previous results for the lower mass targets: triangles, Ref. 4; squares, Ref. 3; and open circles, Ref. 2. Results of the Glauber calculation of the charge exchange cross sections are plotted with the symbol ◆.

of the two cross sections for values of $A \geq 27$ led us to attempt a fit of the form $d\sigma/d\Omega = \alpha A^{\beta}$. The values of the parameters extracted from the data of the present experiment are given in Table IV, and the fits are plotted in Fig. 6 for $A \geq 27$. The cross section for the charge exchange region is seen to vary as $A^{2/3}$ whereas the valley and pion regions vary as $A^{1/2}$. Fits using the neutron number $\bar{N}$ instead of A were also tried and the values of the parameters extracted are listed in Table IV. These fits have slightly worse values of χ^2 than those using A.

TABLE IV. Values of parameters extracted from power law fits: αA^{β} and γN^{δ}.

Region	α	β	γ	δ
CEX	6.49	0.671	11.5	0.622
Valley	0.042	0.47	0.062	0.44
Pion	60.3	0.465	89.6	0.432

Previous experiments[5,13] at lower energy (143 and and 340 MeV, too low for appreciable pion production) have indicated that integral neutron yields near 0° vary roughly as $N^{2/3}$, in qualitative agreement with the results obtained for the CEX region in the present experiment.

The integrated charge exchange cross section for each nucleus has been calculated in a Glauber model[14] that includes attenuation effects due to absorption of the incident beam and outgoing neutron. Knowledge of both the neutron and proton densities is needed in the calculation, which is formulated in terms of a thickness function, defined by Glauber as

$$T(b) = \int_{-\infty}^{+\infty} \rho[(z^2 + b^2)^{1/2}]dz,$$

where ρ is either the proton or neutron density and b is an impact parameter. The nuclear charge exchange cross section is then expressed as

$$\frac{d\sigma^{\mathrm{CEX}}}{d\Omega} = \frac{d\sigma^{\mathrm{CEX}}}{d\Omega_{\mathrm{free}}} N\left[\int e^{-\sigma_{\mathrm{tot}}[T'_n(b)+T_p(b)]} \frac{T_n(b)}{N}\, d^2b - \left(\int e^{-\sigma_{\mathrm{tot}}/2[T'_n(b)+T_p(b)]} \frac{T_n(b)}{N}\, d^2b\right)^2 + \frac{(N-Z)}{N}\left(\int e^{-\sigma_{\mathrm{tot}}/2[T'_n(b)+T_p(b)]} \frac{T_n(b)}{N}\, d^2b\right)^2\right]. \quad (1)$$

where T_n and T_p are the neutron and proton thickness functions, respectively, and $T'_n = [(N-1)/N]T_n$. T'_n is used in the exponent since a nucleon inside a nucleus cannot screen itself. The cross section σ_{tot} is the average of the neutron and proton total nucleon cross sections. In the present calculation the proton and neutron density distributions are assumed to be equal and are described by a Woods-Saxon form. The results of this calculation are plotted in Fig. 6 and, although the overlap with the data is poor, there is qualitative agreement with the trend of the measured cross sections. The calculation has two contributions, one being an incoherent component given by the first two integrals in Eq. (1) resulting from the charge exchange interaction of each neutron with the incident proton. A second component is given by the last integral in Eq. (1) which represents the coherent transition to the isobaric analog state. The latter is approximately 14% of the entire CEX cross section (for $A \geq 27$) and reflects the fact that the coefficient of the free cross section for the coherent component in Eq. (1) is of the order one.

We would like to express our gratitude to the staff of LAMPF for their help, which was essential to the performance of this experiment. We also thank R. J. Glauber for his interest in the results and for conversations concerning their interpretation.

*Work supported under the auspices of the U. S. Energy Research and Development Administration.

†Present address: Los Alamos Scientific Laboratory, University of California, Los Alamos, New Mexico 87545.

[1]G. Glass *et al.*, Phys. Rev. D 15, 36 (1977).
[2]C. W. Bjork *et al.*, Phys. Lett. 63B, 31 (1976).
[3]P. J. Riley *et al.*, Phys. Lett. 68B, 217 (1977).
[4]C. G. Cassapakis *et al.*, Phys. Lett. 63B, 35 (1976).
[5]P. H. Bowen *et al.*, Nucl. Phys. 30, 475 (1962).
[6]C. J. Batty *et al.*, Nucl. Phys. A116, 643 (1968).
[7]R. Madey and F. M. Waterman, Phys. Rev. C 8, 2412 (1973).
[8]F. M. Waterman and R. Madey, Phys. Rev. C 8, 2419 (1973).
[9]G. D. Harp, Phys. Rev. C 10, 2387 (1974).
[10]H. W. Bertini, Phys. Rev. C 6, 631 (1972); 188, 1711 (1969).
[11]B. E. Bonner *et al.*, in Proceedings of the Second International Conference on the *NN* Interaction, Vancouver, 1977 (AIP, New York, to be published).
[12]P. J. Tallerico, Los Alamos Scientific Laboratory Report No. LA-UR-900, 1974 (unpublished).
[13]W. J. Knox *et al.*, Phys. Rev. 81, 687 (1951).
[14]R. J. Glauber, in *Proceedings of the International Conference on High Energy and Nuclear Structure, Columbia University, New York, 1969* (Plenum, New York, 1970), p. 207.